

Charge-sensing of a Ge/Si core/shell nanowire double quantum dot using a high-impedance superconducting resonator

J. H. Ungerer,^{1,2,*} P. Chevalier Kwon,^{1,*} T. Patlatiuk,¹ J. Ridderbos,^{1,3} A. Kononov,¹
D. Sarmah,¹ E. P. A. M. Bakkers,^{4,5} D. Zumbühl,^{1,2} and C. Schönenberger^{1,2,†}

¹*Department of Physics, University of Basel, Klingelbergstrasse 82 CH-4056, Switzerland*

²*Swiss Nanoscience Institute, University of Basel, Klingelbergstrasse 82 CH-4056, Switzerland*

³*MESA+ Institute for Nanotechnology, University of Twente,
P.O. Box 217, 7500 AE Enschede, The Netherlands*

⁴*Kavli Institute of Nanoscience, Delft University of Technology, Lorentzweg 1, 2628 CJ Delft, The Netherlands*

⁵*Department of Applied Physics, TU Eindhoven,
Den Dolech 2, 5612 AZ Eindhoven, The Netherlands*

(Dated: December 6, 2022)

Spin qubits in germanium are a promising contender for scalable quantum computers. Reading out of the spin and charge configuration of quantum dots formed in Ge/Si core/shell nanowires is typically performed by measuring the current through the nanowire. Here, we demonstrate a more versatile approach on investigating the charge configuration of these quantum dots. We employ a high-impedance, magnetic-field resilient superconducting resonator based on NbTiN and couple it to a double quantum dot in a Ge/Si nanowire. This allows us to dispersively detect charging effects, even in the regime where the nanowire is fully pinched off and no direct current is present. Furthermore, by increasing the electro-chemical potential far beyond the nanowire pinch-off, we observe indications for depleting the last hole in the quantum dot by using the second quantum dot as a charge sensor. This work opens the door for dispersive readout and future spin-photon coupling in this system.

I. INTRODUCTION

The interest in group-IV semiconductor spin qubits is large because of their small footprint, a low concentration of nuclear spins and available knowledge about their production in semiconductor industry [1–5]. By integrating on-chip superconducting resonators, strong spin-photon coupling has been demonstrated for spins of confined electrons in a Si two-dimensional electron gas [6, 7]. Hole spins may offer the additional advantages of improved relaxation and decoherence times as they lack a valley degeneracy and exhibit a reduced wavefunction overlap with nuclear spins [8, 9]. Especially, holes in one-dimensional Si or Ge nanowires [10–12] are of a special interest because they possess strong spin-orbit interaction [13–15]. The spin-orbit interaction potentially simplifies qubit control and coupling to resonators by electric-dipole spin resonance (EDSR) [16, 17]. It thereby releases the need of implementing micromagnets and hence facilitates scaling-up.

Recently, the coherent manipulation of a hole-spin qubit in a gate-defined double quantum dot (DQD) in a Ge/Si core/shell nanowire has been demonstrated [18]. However, in these experiments both the charge and the spin-state of the double quantum dot were determined by direct current measurements. This technique limits the capability of determining the total number of holes present in the nanowire. Furthermore, it requires long

integration times and severely limits the maximum cycle length in pulsed-gate experiments.

Rather than measuring the current through the Ge/Si core/shell nanowire double quantum dot, pioneering works have employed another quantum dot to determine changes in the charge-occupancy of the DQD and to perform spin readout [19, 20].

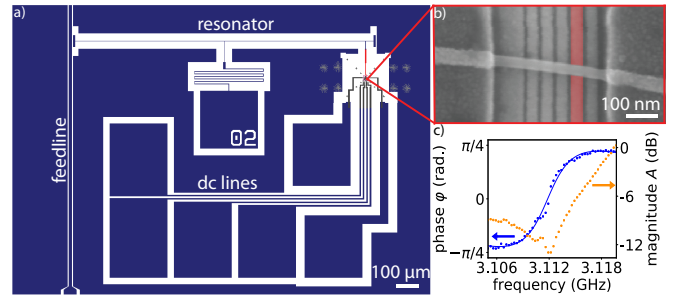


FIG. 1. Device overview. a) Schematic of hybrid resonator architecture. NbTiN is shown in dark blue, the Si substrate is shown white. The feedline on the left is used for reading out the notch-type coplanar-waveguide half-wave resonator which is dc biased at its voltage node in the center. Additional dc lines are used for sending current through the nanowire and applying gate voltages on all bottom gates. b) False colored scanning electron micrograph of a similar device with Ge/Si nanowire lying on top of bottom gates covered with HfO₂. The gate colored red is connected to the resonator. c) Transmission (phase and magnitude) through the feedline as a function of frequency close to the resonator frequency. The solid blue curve indicates a fit from which we extract the resonance frequency and estimate the quality factor (see main text).

* These authors contributed equally to the work.

† www.nanoelectronics.unibas.ch

A different approach for measuring the DQD is realized by probing a resonator coupled to the source contact of a DQD [21–23]. This approach is further simplified by connecting the resonator to a plunger gate, performing gate-dispersive sensing [24]. This technique has enabled measurements of the relaxation and dephasing times of hole spins in a Ge/Si core/shell nanowire DQD using a lumped-element resonator [25]. First attempts of coupling Ge/Si nanowires to on-chip superconducting resonators were based on low-impedance resonators with a weak charge-photon coupling and in a regime of many holes present in the nanowire [26].

In this work, we extend the existing measurements by coupling one of the two quantum dots to a high-impedance superconducting resonator, see Fig. 1. The used coupling scheme allows us to detect charging in the other dot by means of capacitive charge sensing [27–30]. We map the charge-stability diagram using both, direct current measurements and resonator spectroscopy. Furthermore, we gate the nanowire to a regime of low hole occupancy where no direct current through the nanowire can be observed (pinch-off). In this regime, the resonator spectroscopy signal reveals the presence of several more holes in the investigated dot. Finally, by further increasing the gate voltages, we find indications of the depletion of the last hole in the investigated dot.

II. DEVICE DESCRIPTION

An overview of the device under investigation is shown in Fig. 1a) and b). The device consists of a hybrid resonator-nanowire architecture. A notch-type half-wave ($\lambda/2$) resonator with a central frequency $f_r \approx 3.1$ GHz is defined in a NbTiN film of thickness ~ 10 nm, center conductor width of ~ 370 nm and a distance between center conductor and ground plane of ~ 35 μ m. The resonator is capacitively coupled at a voltage anti-node to a feedline which is used for resonator readout. At the middle of the center conductor (voltage node), the resonator is dc biased. In front of the dc bias pad, a meandered inductor ensures sufficient frequency detuning between the $\lambda/2$ mode and a second, quarter-wave mode that forms due to the T-shaped section of the resonator. Thereby, microwave-leakage through the dc bias line is reduced [31]. The resonator's second voltage anti-node is galvanically connected to one out of five bottom gates. The bottom gates are fabricated by Ti/Pd sandwiched by ALD-grown HfO₂ and have a width of approximately 25 nm. The gate pitch is 50 nm. On top of the bottom gates a Ge/Si core/shell nanowire is deterministically placed using a micromanipulator, see Fig. 1 b). All presented measurements are performed in a dilution refrigerator at a base temperature of 35 mK.

The transmission S_{21} through the feedline in proximity to the notch-type resonator as a function of frequency f is given by [32, 33]

$$S_{21}(f) = ae^{i\alpha}e^{-2\pi if\tau} \left[1 - \frac{e^{i\Phi}/(1+Q_c/Q_{\text{loss}})}{1+2i(f/f_r-1)/(1/Q_c+1/Q_{\text{loss}})} \right],$$

where a , α and τ account for the microwave propagation through the wiring in the cryostat and the resonance is described by its resonance frequency f_r , the coupling quality factor Q_c and the loss quality factor Q_{loss} . The term $e^{i\Phi}$ accounts for the Fano shape of the observed resonance arising from impedance mismatches in the feedline coupled to the resonator [34].

We identify the resonance of the superconducting resonator at around 3.1 GHz by considering its temperature dependence. The measured transmission (phase and magnitude) through the feedline around resonance is shown on Fig. 1c). The signal is superimposed on a large standing-wave background (see Fig. A.1 in the appendix.) which we attribute to an impedance mismatch between the feedline and the 50-Ohm environment of the cryostat. Despite the large fluctuations in the transmission magnitude, we are able to fit the phase of the transmission (solid, blue curve in Fig. 1c) and extract the resonance frequency $f_r = 3.111$ GHz, and estimate the Q factors $Q_c \approx 600$ and $Q_{\text{loss}} \approx 600$. The uncertainty in these values originates from the large standing wave background.

We perform a finite-element simulation of the resonator using Sonnet and recover the resonance frequency of the central mode of the resonator half-wave mode when taking into account a sheet kinetic inductance of 70 pH/ \square . Together with the stray line capacitance of 75 pF/m, this corresponds to a resonator impedance of 1.6 k Ω , much larger than the standard 50 Ω , hence improving the coupling strength between resonator and double quantum dot [35, 36]. We attribute the rather low Q_{loss} to microwave leakage from the resonator to the dc lines via capacitive coupling through the set of bottom gates [37]. Indeed, using Sonnet, we estimate the mutual capacitance between two neighbouring bottom gates to be $C_{\text{gg}} \approx 800$ aF. In future works, the mutual capacitance can likely be decreased with an optimised gate geometry and the resulting microwave leakage might be further reduced via improved filtering of the dc lines [31, 38].

III. CHARGE SENSING

Due to the Fermi level pinning stemming from the staggered Si/Ge band-gap alignment, the Ge/Si core/shell nanowire is a hole conductor. Therefore, by applying positive gate voltages, we define the barrier potentials on the gates g_1 , g_3 and g_5 . This gives rise to the confinement potential of two quantum dots whose electrochemical potentials are tuned by the gates g_2 and g_4 [39].

In the following, we investigate two different confinement configurations. The first configuration is schematically depicted in Figure 2a). Here, two fairly symmetric quantum dots, the left (L) and the right (R), are formed between the gates g_1 and g_3 and between the gates g_3 and g_5 . In this configuration, each dot couples to its respective neighbors as shown on the sketch in Figure 2a).

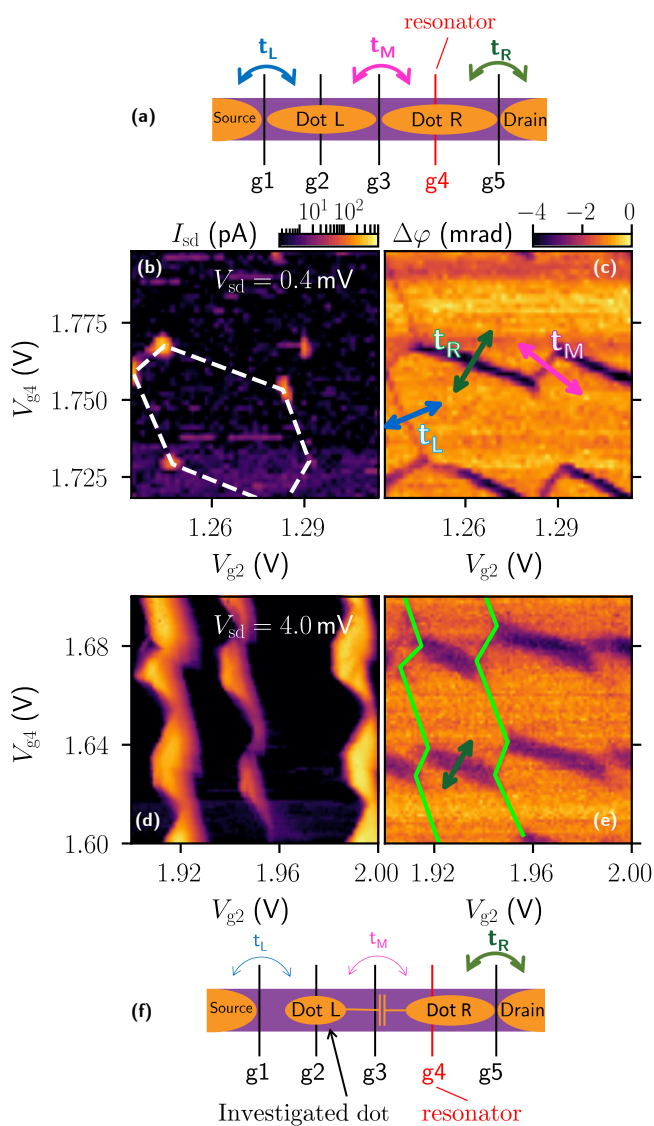


FIG. 2. Charge sensing. a) Schematic of the gate-defined double quantum dot and the relevant tunnel couplings between dots and leads. b) Logarithmic current, I_{sd} , through the nanowire exhibiting the position of triple points. Here, the bias voltage is $V_{sd} = 400 \mu\text{V}$ and the values of the other gate voltages are $V_{g1} = 3.2 \text{ V}$, $V_{g3} = 1.175 \text{ V}$, $V_{g5} = 9.0 \text{ V}$. c) Phase difference, $\Delta\varphi$ of the resonator spectroscopy acquired at the same time as b). Tunnel couplings depicted in a) cause a phase shift of the resonator when any potentials of the system are aligned, as indicated by the colored double arrows corresponding to the tunnel transitions in a). f) Schematic of double quantum dot for a more isolated configuration. d) and e) correspond to b) and c) for the configuration depicted in f). Solid, green lines in e) indicate discharging lines of dot L. Here, the values of the other gate voltages are $V_{g1} = 3.2 \text{ V}$, $V_{g3} = 1.15 \text{ V}$ and $V_{g5} = 9.0 \text{ V}$. The bias voltage is $V_{sd} = 4 \text{ mV}$ and therefore bias triangles appear larger in e) compared to b). The microwave power at the input of the feedline is $\sim -60 \text{ dBm}$ for both measurements.

In Figure 2b), we plot a measurement of the direct cur-

	2a,b,c)	2d,e,f)
$C_{g2,dL}$ (aF)	3.4 ± 0.4	5.4 ± 0.8
$C_{g4,dL}$ (aF)	0.2 ± 0.4	0.8 ± 0.7
$C_{\Sigma,L}$ (aF)	51 ± 19	15 ± 7
$C_{g2,dR}$ (aF)	0.4 ± 0.4	0.1 ± 0.6
$C_{g4,dR}$ (aF)	4.1 ± 0.5	4.1 ± 0.5
$C_{\Sigma,R}$ (aF)	57 ± 20	20 ± 12
C_M (aF)	17 ± 8	8 ± 5

TABLE I. Gate-to-dot capacitances, where C_{g_i,d_j} is the capacitance between gate g_i and dot j ($i \in \{2, 4\}$ and $j \in \{L, R\}$). $C_{\Sigma,j}$ denotes the total capacitance of dot j and C_M is the dot's mutual capacitance.

rent through the nanowire I_{sd} as a function of the voltages on gates $g2$ and $g4$. Because of Coulomb blockade, we measure a finite current through the nanowire only at the triple points at which the electrostatic potential of both dots is aligned with the electrostatic potential of the leads. By connecting the triple points (dashed white lines in Figure 2b)), we find the charge-stability diagram in the shape of a honeycomb pattern [40].

Simultaneously to measuring the current through the nanowire, we send a microwave signal through the feedline at a frequency close to the resonance frequency f_r . We perform dispersive gate sensing by measuring the phase change of the transmitted signal and plot it in Figure 2c) as a function of gate voltages. As the resonator is capacitively coupled to the quantum dots via one of the plunger gates, it is sensitive to their effective admittance [41–43]. Therefore, by sending a signal through the feedline at a frequency close to the resonator frequency, changes in the transmission amplitude and phase can be detected when the quantum dot admittance changes. Indeed, we note that in the plotted phase response, one can clearly identify the honeycomb pattern of the charge-stability diagram. Whenever the electrochemical potential between a dot and its respective lead, or between the two dots, is aligned, a shift in the phase response is observed. The charge-stability diagram that we gain from both dc and rf measurements are well described by a capacitance model [40]. By considering the change of the number of electrons when changing the gate potentials and using the source-drain bias triangles as an absolute energy scale, we fit the data according to the recipe described in Appendix A of Ref. [44]. We extract the capacitances that are specified in Tab. I.

After, having demonstrated the possibility of detecting the charge-stability diagram by means of resonator spectroscopy, we tune the double quantum dot system into the configuration which is schematically depicted in Figure 2f). The main difference to the previous configuration is the larger voltage on the gate $g2$, while the barrier gate voltages V_{g1} and V_{g3} are not changed significantly. This corresponds to a geometrically smaller dot L with a lower number of holes. Hence, the tunneling rate t_L between the source and dot L, as well as the inter-dot tunneling rate t_M are reduced. In this con-

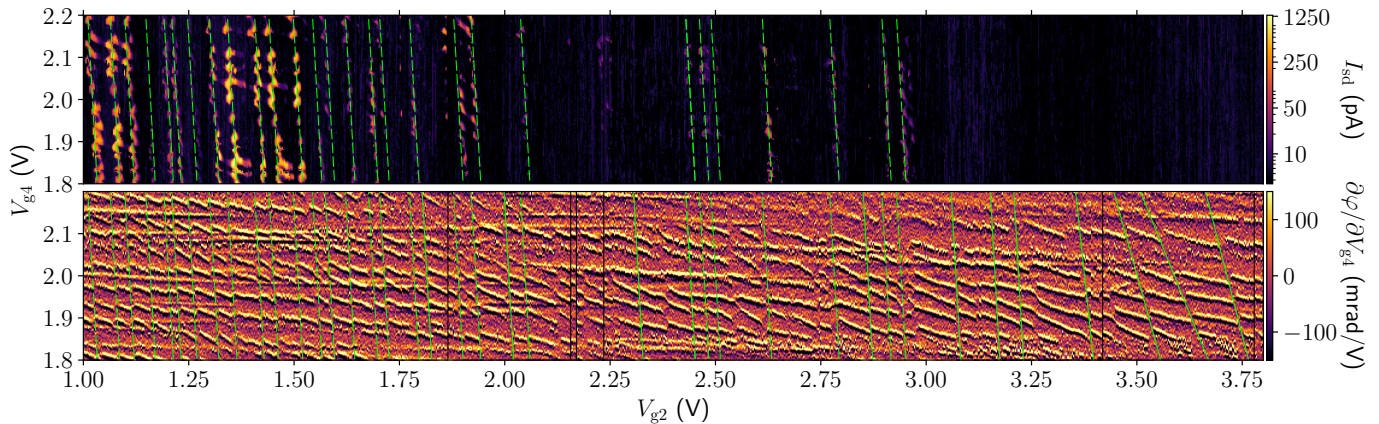


FIG. 3. Nanowire pinch-off. Top panel: map of dc current through the nanowire as a function of gate voltages V_{g2} and V_{g4} , eventually vanishing completely above $V_{g2} \approx 3$ V as the nanowire is pinched off. The positions at which dot 1 is resonant with the lead are highlighted with green, dashed lines. Bottom panel: simultaneously measured resonator spectroscopy, $\partial\varphi/\partial V_{g4}$. The resonator spectroscopy shows the same resonance conditions as in the top panel (green, dashed lines). However, additional transitions are observed (green, solid lines). Gate jumps are marked with vertical, black, solid lines. In this measurement, the other gate voltages are $V_{g1} = 3.2$ V, $V_{g3} = 1.1$ V and $V_{g5} = 9.0$ V and the bias voltage is $V_{sd} = 2$ mV and the readout frequency is $f_{ro} = 3.1259$ GHz.

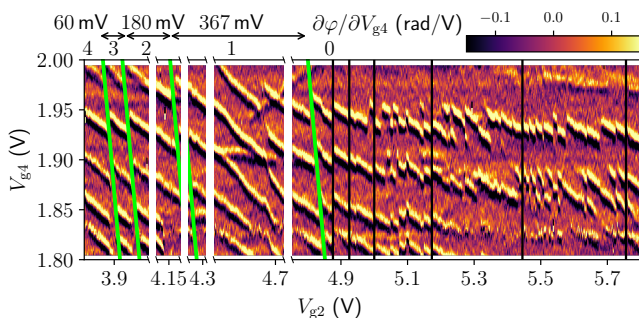


FIG. 4. Indications of last hole depletion. Resonator spectroscopy, $\partial\varphi/\partial V_{g4}$ as a function of gate voltages, V_{g2} , V_{g4} . Resonances correspond to right dot-right lead transition and characteristic discontinuities correspond to hole discharging from the left dot. For gate voltages, $V_{g2} > 4.9$ V, no further regular discontinuities are observed. Instead, random jumps dominate the signal indicating that the last hole has been depleted. The number of holes in the right dot is indicated by a number at the top of the graph. Data repetition due to gate switchers has been omitted in the graph (see supplementary). Here, the other gate voltages are $V_{g1} = 3.2$ V, $V_{g3} = 1.1$ V and $V_{g5} = 9.0$ V. The source drain bias voltage is $V_{sd} = 2$ mV and the readout frequency is $f_{ro} = 3.1259$ GHz.

figuration, it is therefore not possible to measure these transitions using resonator spectroscopy. However, since $V_{g5} = 9.0$ V in both configurations, the remaining tunnel rate t_R is, in first order, not affected, enabling us to use the dot R as a sensor for tracking Coulomb resonances of dot L [27–30]. When we progressively deplete dot L, the tunneling rate between the sensor dot and the drain always remains similar to the resonator frequency. This allows us to track discharging lines of dot L despite the fact that the tunneling involving dot L happens at

much lower frequencies and can therefore not directly be detected by dispersive resonator sensing.

Figure 2d) shows the current through the nanowire in this configuration. We are still able to identify the locations of the triple points in the conductance measurement and calculate the capacitances as given in Table I. Comparison of the conductance with the phase response in Figure 2e) shows that the transmission through the feedline clearly exhibits a change in phase whenever the electrochemical potential of the sensor R is resonant with the one in the drain. We note characteristic jumps in the observed resonances. These jumps correspond to discharging of a hole in the dot L. Therefore, by interconnecting jumps (green lines in Figure 2f)), we determine the Coulomb resonances of the dot L.

The top panel of Figure 3 shows the current through the nanowire in a large range of V_{g2} in the same configuration as Figure 2f). Coulomb resonances of the dot L that are observable in the current are highlighted by dashed, green lines. We note that when considering only the current, the largest gate voltage, at which a Coulomb resonance of dot L is observed, is $V_{g2} \approx 3$ V. When examining the simultaneously measured resonator response in the bottom panel of Figure 3, we identify several transitions that correspond to the sensor being in resonance with the drain. Here, for better visibility, we plot the derivative of the phase response with respect to the gate voltage V_{g4} . These sloped lines have kinks upon removing a hole from dot L because of the dots mutual capacitance. Therefore, by interconnecting the kinks, a Coulomb resonance of dot L is found. We identify several more Coulomb resonances of the dot L than in the dc measurement. Note that the observed Coulomb resonances, highlighted by solid green lines, have a finite slope of $m = \Delta V_{g4}/\Delta V_{g2} \approx -18$ because of a finite capacitance between gate $g4$ and dot L.

The slope corresponding to these transitions changes for voltages $V_{g2} \gtrsim 3.4$ V. This might be related to an (imperfect) potential landscape that makes the dot move to another equilibrium position below a certain number of holes. The slope corresponding to the last transition is $m = \Delta V_{g4}/\Delta V_{g2} \approx -3.9$ and remains the same subsequently, as shown in Figure 4.

Inadvertent charge switching events occurring during this measurement can be rather easily identified because they happen suddenly, at a time scale smaller than the acquisition time of a single data point. Such a single event appears as a (vertical) jump in gate voltage shifting the data along the entire axis, which we refer to as a gate jump from here on. Some of these gate jumps are indicated by vertical, black lines in the figures (e.g. around $V_{g2} \approx 2.2$ V in Fig. 3). Even for gate voltages V_{g2} much larger than the nanowire pinch-off current at 3 V, several Coulomb resonances are found which cannot be identified when only considering the current through the nanowire. We note that in the lower panel of Fig 3, several horizontal features without any kinks are visible. These are interpreted to originate from impurities coupling to the resonator, independent of the quantum dots.

Finally, with the goal in mind to deplete the last hole from dot L, we tune the gates into a third configuration in which we increase V_{g1} from 3.1 V to 5.8 V. In this configuration, the nanowire is fully pinched-off and a direct current cannot be measured. In Figure 4, we plot the derivative of the phase on the resonator signal with respect to the gate voltage V_{g4} as a function of V_{g2} and V_{g4} . Once again, we identify resonances corresponding to tunnelling between dot R and the drain. When connecting the characteristic shifts of these resonances, we obtain the parallel discharging lines (solid, green lines in Figure 4) of the dot L.

Since we work with larger gate voltages and thus a decreasing number of charges present in the wire, there is less screening and the wire becomes less stable, suffering from several gate jumps. These gate jumps result in shifts along the V_{g2} -axis towards less positive voltages. In order to focus on the physics that corresponds to discharging of the dot L, those shifts are removed in Figure 4 where the removed regions are also clearly marked. For completeness, the full data set can be found in Fig. A.2 in the appendix. In Figure 4, we observe a total of four sloped, parallel lines; each corresponding to discharging of a single hole from the dot L. The last charging line is found at $V_{g2} = 4.90$ V, showing the position of the 1 to 0 hole transition in dot L, while the penultimate charging line is observed at $V_{g2} = 4.2$ V (bottom axis) indicating the 2 to 1 hole transition. We note that even after subtracting the additional voltage range, because of shifts along the V_{g2} -axis due to gate jumps, the effective voltage distance between these two lines is $\Delta V_{g2} \approx 370$ mV, much larger than the distance between any two previous discharging lines.

For voltages larger than $V_{g2} = 4.80$ V, beyond the last observed discharging line, the amount of gate jumps in-

creases drastically. They randomly shift the observed resonances in the gate-gate map and yield vertical disruptions of dot-lead resonances, even within a single vertical gate sweep (fast scan axis). We therefore conclude that they correspond to the random charging and discharging of unwanted charge traps in proximity to the nanowire. The absence of any further dot discharging lines appearing with a slope can give some confidence that indeed, the last hole was depleted from the left dot. We speculate that after depletion of the last hole from the dot, the sensor is more susceptible to unwanted charge traps as the screening by dot L vanishes. Hence, the increase of random gate jumps is consistent with the interpretation that the discharging line at $V_{g2} = 4.80$ V may correspond to discharging of the last hole.

To conclude, we demonstrate charge sensing of a Ge/Si core/shell nanowire double quantum dot by using a superconducting, high-impedance, on-chip NbTiN resonator. Using bottom gates, we are able to define a double quantum dot in the nanowire and consistently map the characteristic charge-stability diagram by both direct current measurements and resonator spectroscopy.

By changing the electrostatic potentials on the gates, we tune the double quantum dot into a regime of a more isolated dot and a second, sensor dot which together with the resonator, we employ as a charge sensor of the first dot. By increasing the gate voltages, we consecutively deplete holes from the dot. We find that even in the regime where no current through the nanowire could be detected, because it is pinched-off, the sensor reveals several more hole discharging events while increasing the gate voltages. Finally, we find indications of the depletion of the last hole from the nanowire. Our measurements confirm that observing only the direct current through these type of nanowires is not a sufficient criterion for counting the absolute number of holes present in a quantum dot in Ge/Si core/shell nanowires.

The circuit-quantum electrodynamics architecture presented in this manuscript lays the foundations for realizing coherent charge-photon and spin-photon coupling based on semiconductor nanowires. We expect that a reduction of the gate-gate and resonator-feedline capacitances will result in resonator quality factors by an order of magnitude larger. Frequent gate jumps inhibited using the device as a spin qubit.

However, the charge stability of the system might be improved in the future by working on the quality of the oxides and nanowires. Because similar nanowires as used in this work have been employed as spin qubits [18], we anticipate that the improvements on the resonator in combination with a more stable nanowire device will enable strong charge photon and coherent spin-photon coupling in Ge/Si core/shell nanowires based on intrinsic spin-orbit interaction, as recently achieved in other material platforms [45, 46].

This research was supported by the Swiss Nanoscience Institute (SNI), the Swiss National Science Foundation through grant 192027 and 179024, and the NCCR Spin Qubits in Silicon (NCCR-Spin). We further acknowledge funding from the European Union's Horizon 2020 research and innovation programme, specifically the FET-open project AndQC, agreement No 828948, the

FET-open project TOPSQUAD, agreement No 847471, and the European Microkelvin Platform (EMP), agreement No 824109. We also acknowledge support through the Marie Skłodowska-Curie COFUND grant QUSTEC, grant agreement N° 847471, and the Georg H. Endress foundation.

-
- [1] F. A. Zwanenburg, A. S. Dzurak, A. Morello, M. Y. Simmons, L. C. Hollenberg, G. Klimeck, S. Rogge, S. N. Coppersmith, and M. A. Eriksson, *Reviews of Modern Physics* **85**, 961 (2013), arXiv:1206.5202.
- [2] C. Kloeffel and D. Loss, *Annual Review of Condensed Matter Physics* **4**, 51 (2013).
- [3] L. M. K. Vandersypen, H. Bluhm, J. S. Clarke, A. S. Dzurak, R. Ishihara, A. Morello, D. J. Reilly, L. R. Schreiber, and M. Veldhorst, *npj Quantum Information* **3**, 1 (2017), arXiv:1612.05936.
- [4] G. Scappucci, C. Kloeffel, F. A. Zwanenburg, D. Loss, M. Myronov, J. J. Zhang, S. De Franceschi, G. Katsaros, and M. Veldhorst, *Nature Reviews Materials* **6**, 926 (2021), arXiv:2004.08133.
- [5] A. Chatterjee, P. Stevenson, S. De Franceschi, A. Morello, N. P. de Leon, and F. Kuemmeth, *Nature Reviews Physics* **3**, 157 (2021).
- [6] X. Mi, M. Benito, S. Putz, D. M. Zajac, J. M. Taylor, G. Burkard, and J. R. Petta, *Nature* **555**, 599 (2018), arXiv:1710.03265.
- [7] N. Samkharadze, G. Zheng, N. Kalhor, D. Brousse, A. Sammak, U. C. Mendes, A. Blais, G. Scappucci, and L. M. Vandersypen, *Science* **359**, 1123 (2018), arXiv:1711.02040.
- [8] C. H. Yang, A. Rossi, R. Ruskov, N. S. Lai, F. A. Mohiyaddin, S. Lee, C. Tahan, G. Klimeck, A. Morello, and A. S. Dzurak, *Nature Communications* **4** (2013), 10.1038/ncomms3069, arXiv:1302.0983.
- [9] J. H. Prechtel, A. V. Kuhlmann, J. Houel, A. Ludwig, S. R. Valentin, A. D. Wieck, and R. J. Warburton, *Nature Materials* **15**, 981 (2016).
- [10] J. Xiang, W. Lu, Y. Hu, Y. Wu, H. Yan, and C. M. Lieber, *Nature* **441**, 489 (2006).
- [11] S. Conesa-Boj, A. Li, S. Koelling, M. Brauns, J. Ridderbos, T. T. Nguyen, M. A. Verheijen, P. M. Koenraad, F. A. Zwanenburg, and E. P. Bakkers, *Nano Letters* **17**, 2259 (2017).
- [12] M. Brauns, J. Ridderbos, A. Li, W. G. Van Der Wiel, E. P. Bakkers, and F. A. Zwanenburg, *Applied Physics Letters* **109**, 143113 (2016).
- [13] C. Kloeffel, M. Trif, and D. Loss, *Physical Review B* **84**, 195314 (2011).
- [14] C. Kloeffel, M. J. Rančić, and D. Loss, *Physical Review B* **97**, 1 (2018), arXiv:1712.03476.
- [15] F. Froning, M. Rančić, B. Hetényi, S. Bosco, M. Rehmann, A. Li, E. P. Bakkers, F. A. Zwanenburg, D. Loss, D. Zumbühl, *et al.*, *Physical Review Research* **3**, 013081 (2021).
- [16] C. Kloeffel, M. Trif, P. Stano, and D. Loss, *Physical Review B - Condensed Matter and Materials Physics* **88**, 1 (2013), arXiv:1306.3596.
- [17] F. Maier, C. Kloeffel, and D. Loss, *Physical Review B - Condensed Matter and Materials Physics* **87**, 1 (2013), arXiv:1302.5027.
- [18] F. N. Froning, L. C. Camenzind, O. A. van der Molen, A. Li, E. P. Bakkers, D. M. Zumbühl, and F. R. Braakman, *Nature Nanotechnology* **16**, 308 (2021).
- [19] Y. Hu, H. O. Churchill, D. J. Reilly, J. Xiang, C. M. Lieber, and C. M. Marcus, *Nature Nanotechnology* **2**, 622 (2007).
- [20] Y. Hu, F. Kuemmeth, C. M. Lieber, and C. M. Marcus, *Nature Nanotechnology* **7**, 47 (2012).
- [21] S. Chorley, J. Wabnig, Z. Penfold-Fitch, K. Petersson, J. Frake, C. Smith, and M. Buitelaar, *Physical Review Letters* **108**, 036802 (2012).
- [22] M. Schroer, M. Jung, K. Petersson, and J. R. Petta, *Physical Review Letters* **109**, 166804 (2012).
- [23] K. Petersson, C. Smith, D. Anderson, P. Atkinson, G. Jones, and D. Ritchie, *Nano Letters* **10**, 2789 (2010).
- [24] J. Colless, A. Mahoney, J. Hornibrook, A. Doherty, H. Lu, A. Gossard, and D. Reilly, *Physical review Letters* **110**, 046805 (2013).
- [25] A. P. Higginbotham, T. Larsen, J. Yao, H. Yan, C. Lieber, C. Marcus, and F. Kuemmeth, *Nano Letters* **14**, 3582 (2014).
- [26] R. Wang, R. S. Deacon, J. Sun, J. Yao, C. M. Lieber, and K. Ishibashi, *Nano Letters* **19**, 1052 (2019).
- [27] L. Hutin, B. Bertrand, E. Chanrion, H. Bohuslavskyi, F. Ansaloni, T.-Y. Yang, J. Michniewicz, D. Niegemann, C. Spence, T. Lundberg, *et al.*, in *2019 IEEE International Electron Devices Meeting (IEDM)* (IEEE, 2019) pp. 37–7.
- [28] F. Ansaloni, A. Chatterjee, H. Bohuslavskyi, B. Bertrand, L. Hutin, M. Vinet, and F. Kuemmeth, *Nature Communications* **11**, 1 (2020).
- [29] E. Chanrion, D. J. Niegemann, B. Bertrand, C. Spence, B. Jadot, J. Li, P.-A. Mortemousque, L. Hutin, R. Maurand, X. Jehl, *et al.*, *Physical Review Applied* **14**, 024066 (2020).
- [30] F. Borjans, X. Mi, and J. Petta, *Physical Review Applied* **15**, 044052 (2021).
- [31] P. Harvey-Collard, G. Zheng, J. Dijkema, N. Samkharadze, A. Sammak, G. Scappucci, and L. M. Vandersypen, *Physical Review Applied* **14**, 1 (2020), arXiv:2005.05411.
- [32] P. J. Petersan and S. M. Anlage, *Journal of Applied Physics* **84**, 3392 (1998).
- [33] S. Probst, F. B. Song, P. A. Bushev, A. V. Ustinov, and M. Weides, *Review of Scientific Instruments* **86** (2015), 10.1063/1.4907935, arXiv:1410.3365.
- [34] M. S. Khalil, M. J. Stoutimore, F. C. Wellstood, and K. D. Osborn, *Journal of Applied Physics* **111** (2012), 10.1063/1.3692073, arXiv:1108.3117.
- [35] A. Blais, R.-S. Huang, A. Wallraff, S. M. Girvin, and

- R. J. Schoelkopf, *Physical Review A* **69**, 062320 (2004).
- [36] N. Samkharadze, A. Bruno, P. Scarlino, G. Zheng, D. DiVincenzo, L. DiCarlo, and L. Vandersypen, *Physical Review Applied* **5**, 044004 (2016).
- [37] X. Mi, J. V. Cady, D. M. Zajac, J. Stehlik, L. F. Edge, and J. R. Petta, *Applied Physics Letters* **110** (2017), 10.1063/1.4974536, arXiv:1610.05571.
- [38] X. Mi, J. Cady, D. Zajac, J. Stehlik, L. Edge, and J. R. Petta, *Applied Physics Letters* **110**, 043502 (2017).
- [39] F. N. Froning, M. K. Rehmann, J. Ridderbos, M. Brauns, F. A. Zwanenburg, A. Li, E. P. Bakkers, D. M. Zumbühl, and F. R. Braakman, *Applied Physics Letters* **113** (2018), 10.1063/1.5042501, arXiv:1805.02532.
- [40] W. G. Van der Wiel, S. De Franceschi, J. M. Elzerman, T. Fujisawa, S. Tarucha, and L. P. Kouwenhoven, *Reviews of Modern Physics* **75**, 1 (2002).
- [41] M. Delbecq, V. Schmitt, F. Parmentier, N. Roch, J. Vienneot, G. Fève, B. Huard, C. Mora, A. Cottet, and T. Kontos, *Physical Review Letters* **107**, 256804 (2011).
- [42] T. Frey, P. J. Leek, M. Beck, A. Blais, T. Ihn, K. Ensslin, and A. Wallraff, *Physical Review Letters* **108**, 1 (2012), arXiv:1108.5378.
- [43] V. Ranjan, G. Puebla-Hellmann, M. Jung, T. Hasler, A. Nunnenkamp, M. Muoth, C. Hierold, A. Wallraff, and C. Schönenberger, *Nature Communications* **6**, 1 (2015).
- [44] P. Scarlino, J. H. Ungerer, D. J. van Woerkom, M. Mancini, P. Stano, C. Müller, A. J. Landig, J. V. Koski, C. Reichl, W. Wegscheider, T. Ihn, K. Ensslin, and A. Wallraff, *Phys. Rev. X* **12**, 031004 (2022).
- [45] C. X. Yu, S. Zihlmann, J. C. Abadillo-Uriel, V. P. Michal, N. Rambal, H. Niebojewski, T. Bedecarrats, M. Vinet, E. Dumur, M. Filippone, *et al.*, arXiv preprint arXiv:2206.14082 (2022).
- [46] J. H. Ungerer, A. Pally, A. Kononov, S. Lehmann, J. Ridderbos, K. A. Dick, C. Thelander, V. Maisi, P. Scarlino, A. Baumgartner, and C. Schoenenberger, in preparation (2022).

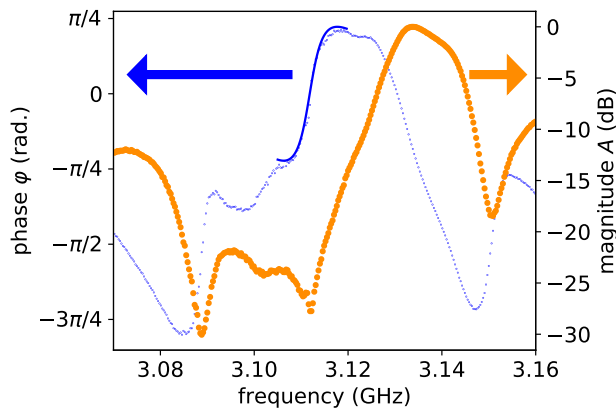


FIG. A.1. Transmission through the feedline in wide frequency range

ADDITIONAL DATA

In Figure 1 in the main text, we show the resonance curve of the resonator. When looking at a wider spectral range, which is shown in Fig. A.1, it becomes apparent that the resonance is superimposed on a large standing wave background. Nonetheless, the resonator can be identified by considering a temperature-dependence scan, because its resonance frequency depends on the the large temperature-dependent kinetic inductance.

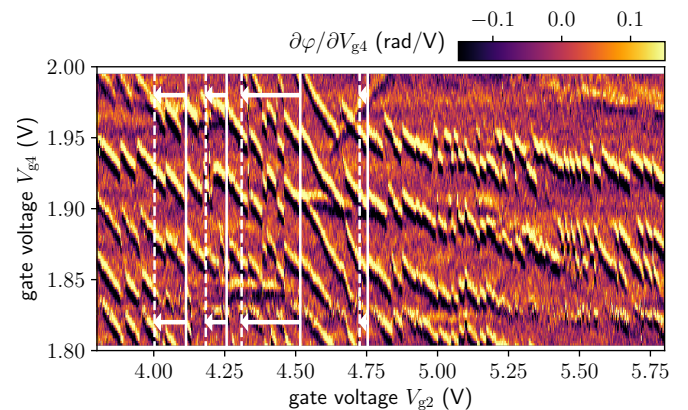


FIG. A.2. Resonator response as a function of gate voltage V_{g2} and V_{g4} . This data set was used to create Fig. 4. The solid, white lines show the positions of the gate jumps. In Fig. 4, the data between the white, solid lines and the white, dashed lines, indicated by arrows, was omitted.

During the measurement of the data presented in Fig. 4 in the main text, several gate jumps occurred. These gate jumps result in shifts along the V_{g2} -axis. In order to focus on the relevant physics, we have omitted those shifts in Fig. 4. Fig. A.2 shows the complete data set where white annotations highlight which data was omitted in Fig. 4 (see caption of the figure).